ORIGINAL RESEARCH Open access

Radiation Modeling in Agrivoltaic Greenhouses Using Semi-Transparent Photovoltaic Algorithms

Charlotte Dupuis[1*], Hugo Perrin[1], Elise Morel[2], Thomas Martin[3]

Abstract

Solar radiation is an essential element in agrivoltaics applied to greenhouse environments. The way radiation is affected varies depending on the photovoltaic category embedded in greenhouses, which operate through shading. Shading in greenhouses may be beneficial or harmful, making its assessment critical. This investigation outlines refinements and adaptations to an algorithm that computes the shading produced by photovoltaic structures within greenhouses. One central adaptation concerns computing shading from semi-transparent photovoltaic panels, rather than the algorithm's initial formulation, which treated them as completely opaque. Verification of the algorithm was performed using radiation readings captured by pyranometers in a greenhouse setting. The statistical indicators applied were Pearson's r correlation coefficient, alongside the Coefficient of Variation. Correlation coefficient values recorded during intervals free from shading influence closely matched those documented for the configuration lacking rooftop photovoltaic installations. At the same time, judging by the coefficients of variation, the consistency of radiation distribution throughout the shaded zone was confirmed, consequently substantiating its occurrence. In closing, the influence of semi-transparent photovoltaic structures on Global Horizontal Irradiance and Photosynthetically Active Radiation was explored, revealing decreases of approximately 52% for the first measure and 60% for the second. These modifications to radiation patterns may be either favorable or unfavorable, depending on the crop variety and the greenhouse's operational demands, such as temperature reduction.

Keywords Shading, Algorithm, Semi-transparent photovoltaics, Global horizontal irradiance, Photosynthetically active radiation, Agrivoltaics

*Correspondence:
Charlotte Dupuis
charlotte.dupuis@univ-lille.fr
[1] Department of AI for Endive and Chicory Forcing Cultivation, Faculty of Agriculture, University of Lille, Lille, France
[2] Department of Machine Learning for Sprout and Microgreen Growth Modeling, Faculty of Agriculture, University of Montpellier, Montpellier, France
[3] Department of Smart Substrate Moisture Control, Faculty of Agriculture, University of Nantes, Nantes, France

Introduction

In our previous publication [1], we developed an algorithm that enables users to determine the shaded region produced by photovoltaic modules installed on a greenhouse rooftop. Considering the swift evolution of Agrivoltaics, and more specifically their deployment in greenhouse settings, examining every parameter that this practice may influence becomes indispensable.

Agrivoltaics represents an outstanding approach for uniting electricity generation with food cultivation upon a single land area. This technique maintains direct connections to strategies for shifting away from fossil-fuel reliance for power generation toward more environmentally friendly alternatives, the farming industry, and long-term ecological balance. Simultaneously, it might offer a perfect sphere for investigation and advancement, while fostering new job prospects. The

This is an open access article distributed under the terms of the Creative Commons Attribution-NonCommercial-ShareAlike 4.0 International License (CC BY-NC-SA 4.0), which permits non-commercial use, distribution, reproduction, and adaptation in any medium or format, provided that appropriate credit is given to the original author(s) and source, a link to the license is provided, and any changes made are indicated. Adapted material must be distributed under the same license.

© 2024 The Author(s). | Published by Agro Intelligence Research Press

capabilities inherent in Agrivoltaics, understood broadly (Interspersed PV arrays, Greenhouse-mounted PV arrays, Stilt-mounted PV arrays [2]), receive emphasis within the technical document [3] issued by the Joint Research Centre of the European Commission, wherein it indicates that rolling out Agrivoltaic arrangements across a mere 1 % of the European Union's Utilized Agricultural Area (UAA) might yield 1 TW of electric power, during an era where the European Union's aspiration for solar power reaches 590 GW before 2030.

Having said that, particularly in a greenhouse context, installing photovoltaic modules on the roof can reshape the microclimate, with solar radiation being the characteristic most strongly altered. Sunlight is the primary power source in a greenhouse and is indispensable for plant growth, as it is central to biological processes such as photosynthesis. The use of opaque or, indeed, cutting-edge semi-transparent photovoltaic modules can modify incoming sunlight, largely through shading.

Shading in greenhouse systems is a cooling strategy routinely employed [4], substantially reducing the thermal energy penetrating through sunlight. In parallel, it may deliver greater benefits to crops that require reduced levels of sunlight radiation to flourish. As highlighted by Caruso *et al.* [5], elevated sunlight intensity, particularly during summer, is a limiting factor for the development of the perennial wall rocket crop. Hence, shading serves as an instrument to boost agricultural output. In contrast, crops in which reduced sunlight radiation impairs their core biological mechanisms are likely to experience adverse consequences, manifested as decreased yield and structural irregularities [6, 7]. To conclude, throughout earlier investigations we undertook examining the shading implications of semi-transparent photovoltaic panels on strawberry plants, we observed that shading simultaneously favored the qualitative advancement of the plants (enhanced total phenolic content and free radical-scavenging activity), while nonetheless yielding diminished fruit mass [8].

That portion of the sunlight spectrum that exerts a considerable influence on crops spans 400-700 nm and constitutes the Photosynthetically Active Radiation (PAR) band. The strongest effect on photosynthesis comes from the 400–500 nm (blue) band, which shows a peak at 440 nm, together with the 600–700 nm (red) band, which displays dual peaks at 620 and 670 nm [9]. Additionally, the blending of these dual sunlight spectra has been investigated, with a 3:1 (red: blue) ratio achieving superior growing conditions [10-12].

Turning to photovoltaics, the materials used to fabricate solar cells vary. A multitude of inquiries address this distinct dimension of Agrivoltaics within greenhouses, with polycrystalline silicon [13, 14], monocrystalline silicon [15], amorphous silicon [16], and organic photovoltaics [17] receiving thorough examination. The foremost distinction separating the aforementioned photovoltaic categories lies in their sensitivity to sunlight, especially PAR. Radiation strength fluctuates across seasons, depending on the rooftop coverage proportion occupied by photovoltaics and, for photovoltaic categories, on the extent of their solar cell coverage. To be precise, as indicated by López-Díaz *et al.* [13], employing rooftop coverage of 15%, 30%, alongside 50%, the PAR diminishment reached 28.8%, 46.6%, alongside 66.3%, respectively, whilst meaningful variations additionally surfaced comparing opaque against semi-transparent photovoltaics, where PAR diminishment measured 43.5% alongside 31.7%, respectively, as indicated by Tang *et al.* [16].

Frameworks formulated in recent times, grounded in the Agrivoltaics paradigm, chiefly address two distinct aspects: the effects of photovoltaics on greenhouse radiation and other microclimatic factors, and the electricity output from photovoltaic arrangements in greenhouses. To elaborate, Torrente *et al.* [18] developed a framework for simulating radiation dispersion throughout a greenhouse equipped with rooftop photovoltaics. Such a framework, which transcends photovoltaics' influence on radiation, also provides data on reference evapotranspiration (ETo). From an electrical standpoint, Pérez-Alonso *et al.* [19] developed a neural network framework capable of projecting the immediate electrical power output. Frameworks of this nature, as noted, prove tremendously beneficial for intricate and non-linear arrangements, exemplified by that uniting a greenhouse with a photovoltaic system.

Throughout this article, each function is reexamined, along with the theoretical foundation underlying the initial algorithm. Furthermore, the alterations undertaken to enhance the algorithm's functionality are described, alongside its expandability

© 2024 The Author(s). | Published by Agro Intelligence Research Press

to larger-dimension greenhouses. Moreover, the methodologies used to corroborate the updated algorithm and its outputs are outlined. The reliable identification of shading from semi-transparent modules now enables the algorithm's application beyond entrepreneurs and greenhouse owners to individuals aiming to investigate supplementary parameters with precision. Such parameters might relate to the greenhouse microclimate, encompassing temperature or biological crop characteristics. Despite the algorithm failing to calculate scattered radiation outright, it still facilitates its approximation, bypassing the need for specialized supplementary apparatus. This is achievable solely by gauging Global Horizontal Irradiance (GHI) and leveraging the algorithm's ability to analyze sunlight radiation across distinct regions within the photovoltaic unit (solar cells, the see-through section of the photovoltaic, and the entire photovoltaic area). Furthermore, independent of spatial accuracy, computing shading at temporal increments as fine as 1 minute provides additional avenues for investigation. To wrap up, the repercussions of photovoltaics on both GHI and PAR are examined.

Materials and Methods

Recap of the original algorithm

According to the description by Petrakis *et al.* [1], the algorithm rests upon astronomical relations and principles, vector mathematics, and geometry. Every component undergoes consideration and application toward crafting a principal function, encompassing five nested functions and four standalone code segments, of which one constitutes an elective capability. The algorithm's outcomes relate to the surface area placed under shade by the photovoltaics (m2), the share this surface represents across the complete area enveloped by the greenhouse (%), the examination concerning whether a chosen coordinate's placement within the greenhouse falls inside or outside the shaded surface (elective capability), whilst concurrently producing visual depictions, specifically one rendered in three dimensions alongside another in two dimensions, which illustrate the greenhouse, the photovoltaics, together with the prospective shading.

Regarding input variables, the algorithm accepts figures for pinpointing the particular moment the operator requires shading computation (year, month, day, hour, minute, along with time zone), figures describing greenhouse traits (alignment, quantity of structural modules, across width as well as length, structural module length along with width, gutter together with ridge height), the longitudinal together with latitudinal coordinates for establishing the greenhouse's geographic position, and concluding with figures covering the dimensions (length along with width) together with the placement of the photovoltaic modules upon the greenhouse rooftop. One ought to note that, in its original state, the algorithm could produce outcomes every 10 minutes spanning the entire yearly cycle.

As described earlier, the algorithm is built from five nested functions along with four standalone code sections. Function 1 is tasked with finding the Sun's location in spherical coordinates through two fundamental angles—the Solar Zenith Angle (SZA) and the Solar Azimuth Angle (SAA). Given that the entire output rests on the Cartesian coordinate framework, the role of Function 2 lies in figuring out the Earth–Sun distance, r, a quantity later used to switch the Sun's position out of a spherical system $S(r,\theta,\varphi)$ and into a Cartesian one $C(x,y,z)$ (Function 3). The fourth function of the algorithm (Function 4) handles the coordinate determination for the greenhouse, drawing on elementary geometric ties that involve the greenhouse's construction unit measurements alongside iterative "for" loops coded in MATLAB. The closing function (Function 5) works out the vertices that outline the shadow cast by the photovoltaic units. What emerges from this function is the identification of four points lying on the xy-plane (the ground), each corresponding to a corner of the produced shadow. Since the photovoltaic surfaces are flat and, given the chosen shadow-finding approach, pinpointing these four points is sufficient, the projected shadow always assumes a quadrilateral shape on the xy-plane. Taken together, the functions and code sections form a chain, with each output feeding directly into the next step.

Sitting between the 4th and 5th functions, one finds the first separate code section (Part of code 1), which computes the PV coordinates across the greenhouse rooftop. The vast assortment of commercially available photovoltaic modules means this part cannot be cast as a generic function; hence, within this algorithm, the PV positional coordinates were derived to match the actual experimental layout. The second code section splits into two subsections (Part of code 2A and Part of code 2B). These serve to visually render the greenhouse and the shaded zones, respectively. The underlying

© 2024 The Author(s). | Published by Agro Intelligence Research Press

mechanism relies on binary processing—arrays filled with logical 0s and 1s are built, with each cell representing a 1 cm² ground patch. Put differently, running the algorithm constructs a pair of distinct arrays: one maps the greenhouse, assigning 1 to every cell covered by the structure and 0 elsewhere; the other maps the shade, assigning 1 to every cell lying under shadow and 0 elsewhere. The third code section tackles the computation of the greenhouse's shaded footprint. Working from the outcomes of Parts 2A and 2B and keeping in mind that both resulting arrays share identical row and column counts (same ground extent), cells occupying matching positions in both arrays that carry the logical value 1 directly translate to cm² patches that fall simultaneously inside the greenhouse and inside the shadow region. Accordingly, a total of 131 such coinciding cells gives the area of shadow falling within the greenhouse, expressed in cm². The final, elective function asks the user to supply a coordinate pair (x, y) marking a spot on the ground; the algorithm then tests whether that spot lies within the shaded zone. If no coordinates are provided, the algorithm halts at the previous phase.

Implementation of the algorithm leaned on a genuine even-span greenhouse. Semi-transparent photovoltaic modules have been mounted on its south-facing sloped roof. However, for algorithmic purposes, these modules were treated as opaque, accounting for the entire footprint and outline of the rooftop PVs. Under this premise, algorithm validation was also carried out using GHI measurements collected on a horizontal surface with pyranometers (CMP3 from Kipp & Zonen) after the PV unit surfaces had been covered with an opaque medium.

An exhaustive presentation of the shadow-calculation methodology, the employed equations, sample MATLAB code excerpts from the algorithm, and the validation protocol can be found in our original paper [1].

Experimental setup

The greenhouse that serves as the algorithm's foundation is located at the Plant Physiology Laboratory of the Department of Biology at the University of Patras (38° 17′ 27,9″ N, 21° 47′ 23,9″ E). It is a full-scale even-span structure whose ridge runs East–West, comprising four construction units, each 3.2 m wide and 16.39 m long. Gutter height reaches 3.22 m, while ridge height tops out at 3.9 m. Only two of these four units were utilized for this study—the one occupying the northern end of the overall greenhouse, labelled "Northern Construction Unit or CU 2" **(Figure 1a)**, and an adjacent one, labelled "Southern Construction Unit or CU 1" **(Figure 1b)**. It is worth emphasizing that all results refer to CU 2, as this unit is dedicated to cultivation and outfitted with microclimate recording instruments.

© 2024 The Author(s). | Published by Agro Intelligence Research Press

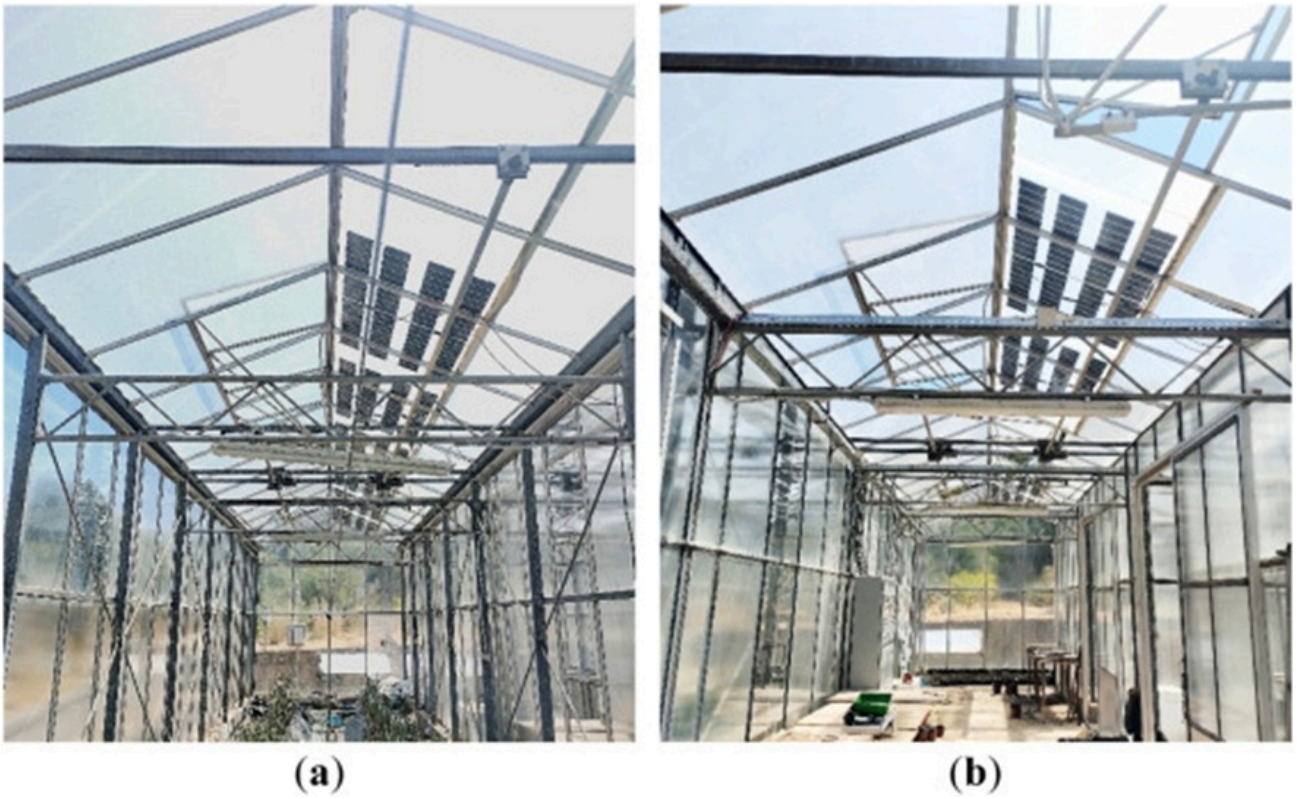

Figure 1. Photovoltaic modules fitted into the south-sloped roof surface of the greenhouse: (a) Northern Construction Unit and (b) Southern Construction Unit.

As for the photovoltaic modules, their hallmark is semi-transparency, with bifacial solar cells sealed between two glass panes. Each module measures 2.089 m long, 1.033 m wide, and 5.5 mm thick. Because of the lengths of both the greenhouse and the photovoltaics, a slight overlap occurred along the short edge of the panels, yielding an effective length of 2.048 m. The total number of solar cells per module is 80, each measuring 166 mm by 83 mm. Their arrangement between the two glass panes consists of four rows of 1.66 m each (20 · 83 mm), with each cell's short side running parallel to the module's long side. The spacing between rows, as well as the margins along the module's width, amounts roughly to 6 cm, 7.5 cm, 10.5 cm, 7.5 cm, and 6 cm, in sequence. Given these figures, the total surface area per module is approximately 2.12 m², with an active area (the combined solar cell surface) of 1.1 m². Hence, the theoretical shading for each unit is roughly 51.9%. **Table 1** collates all specifications for the greenhouse and the PV units used to construct the algorithm.

Table 1. Characteristics of the greenhouse, photovoltaic modules, and solar cells.

Component	Characteristic	Value
Greenhouse	Orientation	East–West
Greenhouse	Number of construction units (widthwise)	2
Greenhouse	Number of construction units (lengthwise)	0
Greenhouse	Width	3.20 m
Greenhouse	Length	16.39 m
Greenhouse	Gutter height	3.22 m

© 2024 The Author(s). | Published by Agro Intelligence Research Press

Greenhouse	Ridge height	3.90 m
Photovoltaic module	Width	1.033 m
Photovoltaic module	Length	2.089 m
Photovoltaic module	Thickness	5.5 mm
Solar cell	Width	83 mm
Solar cell	Length	166 mm
Solar cell	Number	80 pcs
Solar cell	Type	Bifacial Monocrystalline

Finally, placed inside the Northern construction unit stand two CMP3 pyranometers by Kipp & Zonen, recording GHI ($W \cdot m^{-2}$). These pyranometers sit at a height of 0.75 m above ground, at coordinates (xPyr.,1, yPyr.,1) = (4.81, 11.85) and (xPyr.,2, yPyr.,2) = (4.81, 4.55). The coordinates are given in meters, with the lower northwest corner of the greenhouse's southern construction unit as the origin (0, 0). At this same height, two ParLite sensors by Kipp & Zonen record PAR ($\mu mol \cdot m^{-2} \cdot s^{-1}$) on a horizontal plane. Their respective coordinates are (xPAR.,1, yPAR.,1) = (4.71, 11.85) and (xPAR.,2, yPAR.,2) = (4.71, 4.55). This study pairs the above instruments with a CMP3 pyranometer deployed outside the greenhouse.

Improvements and modifications

As noted in Section 2.1, the original algorithm did not account for the semi-transparent nature of photovoltaics. The modules were instead treated as opaque, producing a continuous shadow patch on the ground. Though suitable for a wide range of greenhouse agrivoltaic scenarios—since, until recently, opaque panels predominated—this treatment cannot deliver accurate results for the specific case of semi-transparent photovoltaics, which have become a common choice in recent years. It therefore became necessary to model photovoltaics not as a uniform, opaque plane, but as a plane where opaque solar cells are fixed at precise positions. In the present study, the algorithm was upgraded to account for shading produced not by the entire photovoltaic surface, but solely by its solar cells. **Figure 2** contrasts the earlier representation of the module as an opaque surface (left) with the updated representation as a semi-transparent one (right).

© 2024 The Author(s). | Published by Agro Intelligence Research Press

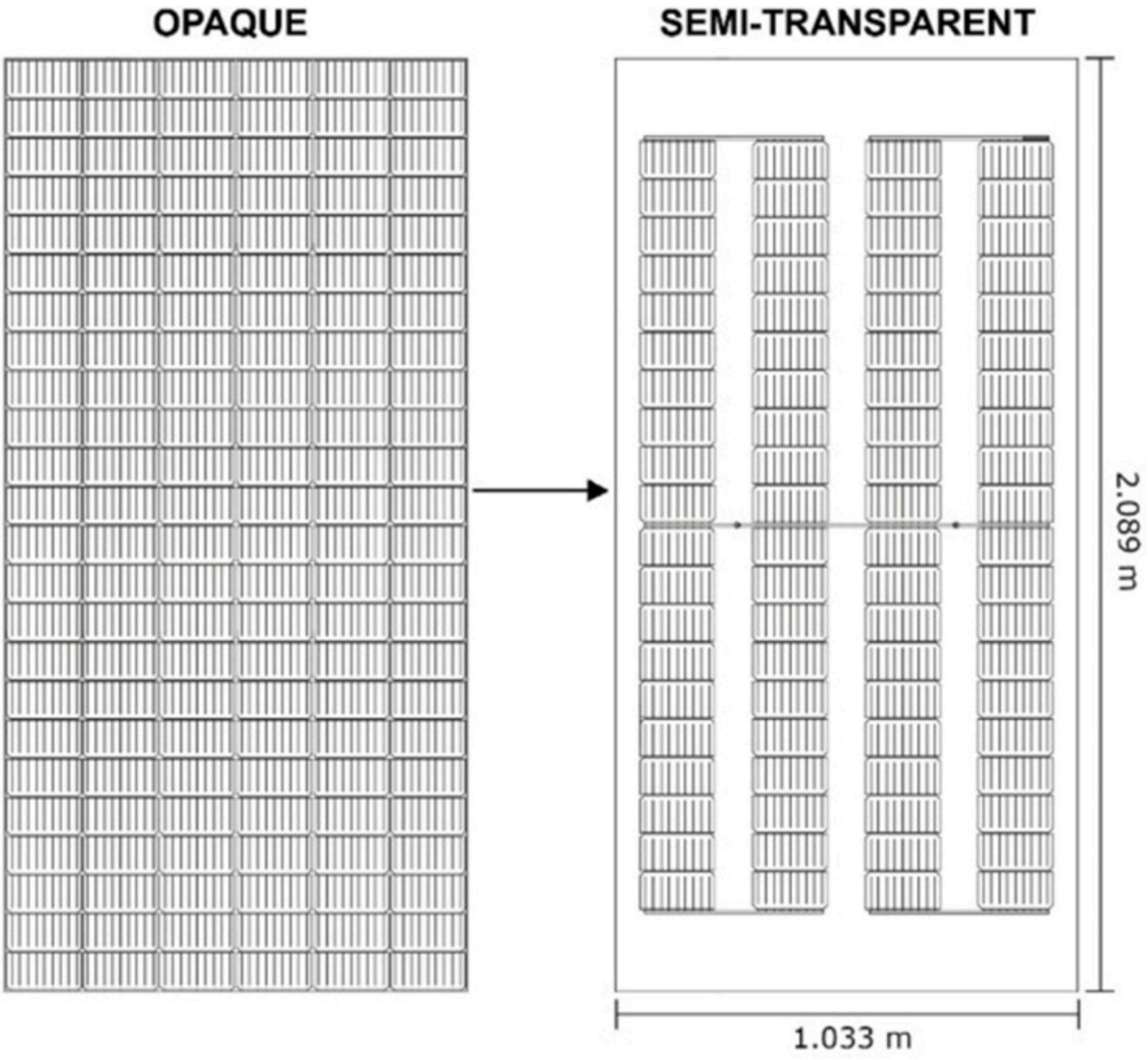

Figure 2. Photovoltaic modules represented as an opaque surface (left) and as a semi-transparent surface (right) [20].

The procedure for calculating the Cartesian coordinates of the solar cells parallels the method used for the photovoltaic module coordinates. As stated, every photovoltaic module contains 80 solar cells, uniformly distributed across 4 rows of 20 cells each. Thus, extra code fragments were introduced into the existing codebase to determine four coordinate triplets (x, y, z) per row (one for each corner of the rectangular cell arrangement), ultimately producing sixteen values along the x-axis, sixteen along the y-axis, and sixteen along the z-axis. These coordinate triplets are computed for each photovoltaic unit mounted on the greenhouse roof.

In the Cartesian coordinate framework, each axis maps to a distinct greenhouse direction. Given that the greenhouse's longer side aligns with the East–West direction, the x-axis captures the North–South direction, the y-axis captures the East–West direction, and the z-axis captures the vertical distance from the ground. Using "for" loops, all needed coordinates are computed as a function of the number of construction units iterated widthwise (index i) and lengthwise (index m), the number of photovoltaic modules (index j), and the number of solar cell rows (index t).

© 2024 The Author(s). | Published by Agro Intelligence Research Press

Another element that was modified is the temporal resolution at which the algorithm computes shading. In its original form, the finest achievable step was 10 min. By incorporating a minutes parameter into the fractional year equation **(Eq. 1)**, the algorithm can now resolve shading down to a minimum time step of 1 min. Specifically, the initially used **Eq. 1** becomes **Eq. 2**. At the same time, the temporal bounds are altered, so that the constraint Minute = [0:10:50] changes to Minute = [0:1:59].

$$\gamma = \frac{2\pi}{365}\left(\mathrm{N} - 1 + \frac{h-12}{24}\right) \quad (1)$$

$$\gamma = \frac{2\pi}{365}\left(\mathrm{N} - 1 + \frac{h-12+\frac{mnt}{24}}{24}\right) \quad (2)$$

Where γ is the fractional year (rad), N is the day of the year—ranging from 1 to 365, or 366 in leap years—and h, together with mnt, represent the required hour and minute of the day, respectively.

A 1 min time step is notably short, given that such rapid variations in solar irradiance do not significantly affect ultimate biomass production. These variations matter when shifts in radiation caused by shading persist for at least one hour over a 24 h span. Yet, daytime solar irradiance may oscillate within seconds due to atmospheric factors, such as cloud cover. Depending on the species, plant stomata respond to changing abiotic conditions within seconds to minutes of stressor onset [21, 22]. Conversely, for species whose stomatal responses are more sluggish—exhibiting time constants greater than those of the abiotic fluctuations—such changes may culminate in plant wilting [23].

Therefore, while the original motivation for this study's finer time-step for shadow detection was to probe solar irradiance with greater precision, the algorithm can now also be employed to investigate responses rooted in biochemical and biophysical physiological pathways that underpin multiple photosynthetic operations, as well as stomatal regulation dynamics.

As stated in Section 2.1, each function or code block takes the output of the preceding function or code block as its own input. Hence, altering the temporal step for shadow computation requires a modest but important adjustment within the function that estimates the Earth–Sun separation (Function 2). Given that Earth requires 365 days to complete a full 365-degree revolution, the angular distance traversed in a single day stands at 0.986°. Extending this logic, across a 1-min span, the angle becomes 0.986°/1440, with 1440 being the count of one-minute intervals within a day. This angle subsequently feeds into the determination of the coordinates (x, y) marking Earth's position along its orbital path around the Sun.

Alongside this, one noteworthy additional feature is the capacity to compute the shaded footprint at assorted elevations. Particularly during early morning and late afternoon, when the Solar Zenith Angle climbs, the shift in shadow placement with height becomes pronounced. Pyranometers installed at heights exceeding 0.5 m (Section 2.2) may consequently fail to capture reliable radiation measurements, especially when their location is near the fringes of the shaded area. In addition to securing dependable radiation data within the scope of this work, the option now exists, through iterative algorithm runs, to construct a thorough three-dimensional map of shading spanning the entire greenhouse interior. This undertaking would likewise serve tall-growing crop varieties well.

More concretely, within the formulas that derive the coordinates of the shaded zone **(Eqs. 3 and 4)**, an extra element representing the targeted shadow elevation, zsh, has been introduced. This quantity is supplied among the algorithm's

© 2024 The Author(s). | Published by Agro Intelligence Research Press

initial input parameters, so that the former equations are converted into **Eqs. 5 and 6**. Resolving these yields coordinate triplets (x, y, z) that match the corner points demarcating the shaded footprint.

$$x_{sh} = x_n - c_n \cdot z_n \quad (3)$$

$$y_{sh} = y_n - \frac{z_n}{b_n} \quad (4)$$

$$x_{sh,\ modified} = x_n - c_n \cdot \left(z_n - z_{sh}\right) \quad (5)$$

$$y_{sh,modified} = y_n - \frac{\left(z_n - z_{sh}\right)}{b_n} \quad (6)$$

Where (x_{sh},y_{sh}) are the shade coordinates originally obtained, $(x_{sh,\ modified},y_{sh,\ modified})$ represent the shade coordinates adapted to the specified shadow height, xn, yn, and zn are the coordinates specifying each corner of the photovoltaic panel, with n = 1, 2, 3, 4, and bn together with cn denote two quantities supplied by **Eqs. 7 and 8**, respectively, in which xs, ys, and zs act as coordinates for fixing the sun's location. The full derivation procedure for **Eqs. 3, 4, 7, and 8** are set out in Petrakis *et al.* [1].

$$b_n = \frac{z_s - z_n}{y_s - y_n} \quad (7)$$

$$c_n = \frac{x_s - x_n}{z_s - z_n} \quad (8)$$

One segment of the code that caused difficulties in the initial version of the algorithm was the binary processing routine. Populating logical arrays intended to portray both the greenhouse and the shade placed a drag on execution speed, thereby undercutting overall efficiency. Assigning one array cell to each square centimeter (a choice driven by the targeted high resolution) yielded arrays of extremely large dimensions, even for a greenhouse occupying a relatively compact footprint. It should be stressed that the algorithm was intended to operate universally, regardless of how many construction units a greenhouse contains or the dimensions of those units. Applied to a vast commercial greenhouse, it would thus become prohibitively unwieldy. Furthermore, certain portions of the algorithm have been extracted to enable multiple runs, delivering all outputs except graphical renderings. Under these conditions, building multiple enormous arrays imposed heavy tolls on processing power and memory.

Prompted by the considerations above, the binary processing segment was replaced with an approach grounded in the MATLAB "boundary" command. Using this command, it suffices to locate only those points forming either the greenhouse's ground footprint or the shaded zone—coordinates already supplied by the earlier functions. The construction of supplementary arrays is thereby eliminated, while precision depends on the number of decimal places the user specifies.

© 2024 The Author(s). | Published by Agro Intelligence Research Press

The logical-array methodology also underpinned verification that an arbitrary point (defined by given coordinates) falls within the shaded footprint. This technique exploited the fact that array rows represented positions along the y-axis, while array columns represented positions along the x-axis. Consequently, provided that both the x-coordinate and the y-coordinate of the query point lay within the ranges of columns and rows carrying a value of 1 (denoting shade presence), the point was classified as belonging to the shaded zone. Failing that, the point lay externally.

This approach was succeeded by a far more straightforward scheme, in which a point is deemed to lie inside a polygon if the sum of the triangular areas formed by the point and each successive vertex of the polygon equals the polygon's overall surface area. If that total area exceeds the polygon's area, the point lies outside the target region. Specifically, and consistent with **Figure 3a**, for a test point I to lie inside region ABCD, the aggregate of areas AIC (E1), AIB (E2), BID (E3), and DIC (E4) must equal the area enclosed by ABCD, in accordance with **Eq. 9**. According to **Figure 3b**, a test point I falls outside region ABCD if the aggregate of areas AIC (E1), AIB (E2), BID (E3), and DIC (E4) surpasses the area enclosed by ABCD, as captured by **Eq. 10**.

$$E_1 + E_2 + E_3 + E_4 = E_{ABCD} \quad (9)$$

$$E_1 + E_2 + E_3 + E_4 > E_{ABCD} \quad (10)$$

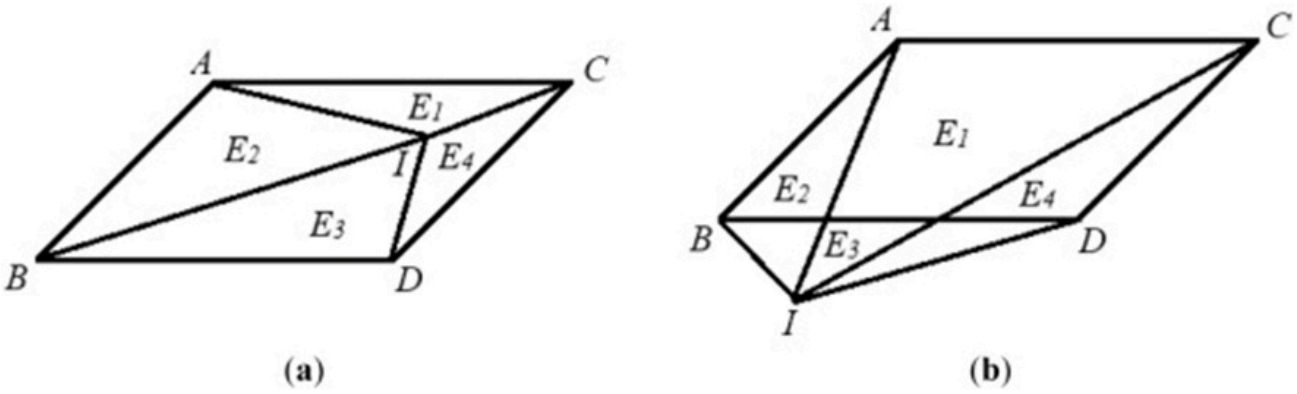

Figure 3. Method for establishing whether a point lies: (a) inside the target region, (b) outside the target region.

Validation method

The original version of the algorithm was corroborated using genuine solar radiation measurements collected via three identical pyranometers (CMP3 by Kipp & Zonen). Two units were placed inside the greenhouse to capture the radiation transmitted through the cover and the photovoltaic panels, while the third unit operated outside to record the radiation incident upon the greenhouse. The metric used to anchor the validation effort was the Coefficient of Variation (CV). Relying on this metric, together with the fact that the gap between outdoor and indoor radiation (GHIexternal – GHIinternal) remained fairly steady in magnitude, the algorithm's accuracy was affirmed whenever a pyranometer lay inside the shaded area it had computed.

For the present study, the same overarching strategy was followed to validate the refined algorithm, specifically drawing on the CV while simultaneously using Pearson's correlation coefficient (r).

© 2024 The Author(s). | Published by Agro Intelligence Research Press

Pearson's r measures the relationship between two datasets; its extreme values of −1 and +1 indicate perfect negative and perfect positive linear association, respectively. A value of zero, by contrast, indicates the absence of correlation between the datasets. Pearson's r is calculated via **Eq. 11**, with xi and yi representing discrete observations of variables x and y, and $\bar{x}$ together with $\bar{y}$ standing for the mean values of those variables. The CV, meanwhile, is characterized as the proportion of the standard deviation (σ) relative to the mean value (μ) **(Eq. 12)**, an expression enabling the pairing of these two descriptors and thereby the spotting of any irregular fluctuations. More specifically, the CV is normally expressed as a percentage, with lower values indicating tighter clustering of the data.

$$r = \frac{\sum_{i=1}^{n}(x_i-\bar{x})(y_i-\bar{y})}{\sqrt{\sum_{i=1}^{n}(x_i-\bar{x})^2}\sqrt{\sum_{i=1}^{n}(y_i-\bar{y})^2}} \quad (11)$$

$$CV = \left(\frac{\sigma}{\mu}\right)\cdot 100\% \quad (12)$$

This work employed one-minute-resolution data spanning nine separate clear-sky days drawn from the April–May–June 2024 quarter. Records preceding sunrise and following sunset were excluded, given the algorithm's inability to fix the sun's position at those times and, therefore, to assess shading. The final count of data points used was 7598. The pyranometers and their respective placements within the greenhouse are detailed in Section 2.2.

To obtain the shaded footprint produced by the photovoltaics, the algorithm was executed for each day included in the analysis, using the greenhouse attributes, photovoltaic module specifications, and solar cell properties collated in **Table 1**, while accounting for the positions and heights of the two pyranometers. The algorithm outputs mobilized for validation comprised the time windows throughout which pyranometers 1 and 2 were:

(ar) situated inside versus outside the zone of influence cast by the full surface of the photovoltaic modules belonging to the northern construction unit

(br) situated inside versus outside the zone of influence cast by the shadow generated from the solar cells of those same PV modules

(cr) situated within the zone of influence of the "transparent" segment of the respective photovoltaic modules.

The three scenarios above are also visualized in **Figure 4**. For scenario (ar), when the pyranometers are within the full photovoltaic surface's influence, they occupy either the red or the green zone. Should this not be the case, the pyranometers reside somewhere in the remaining area (white space). In scenario (br), when the pyranometers are in the shadow of the solar cells, they are in the red zone. Otherwise, they lie within the green zone or elsewhere. Finally, for scenario (cr), when the pyranometers sit within the influence of the "transparent" segment of the photovoltaics, they are located inside the green zone depicted in **Figure 4**.

© 2024 The Author(s). | Published by Agro Intelligence Research Press

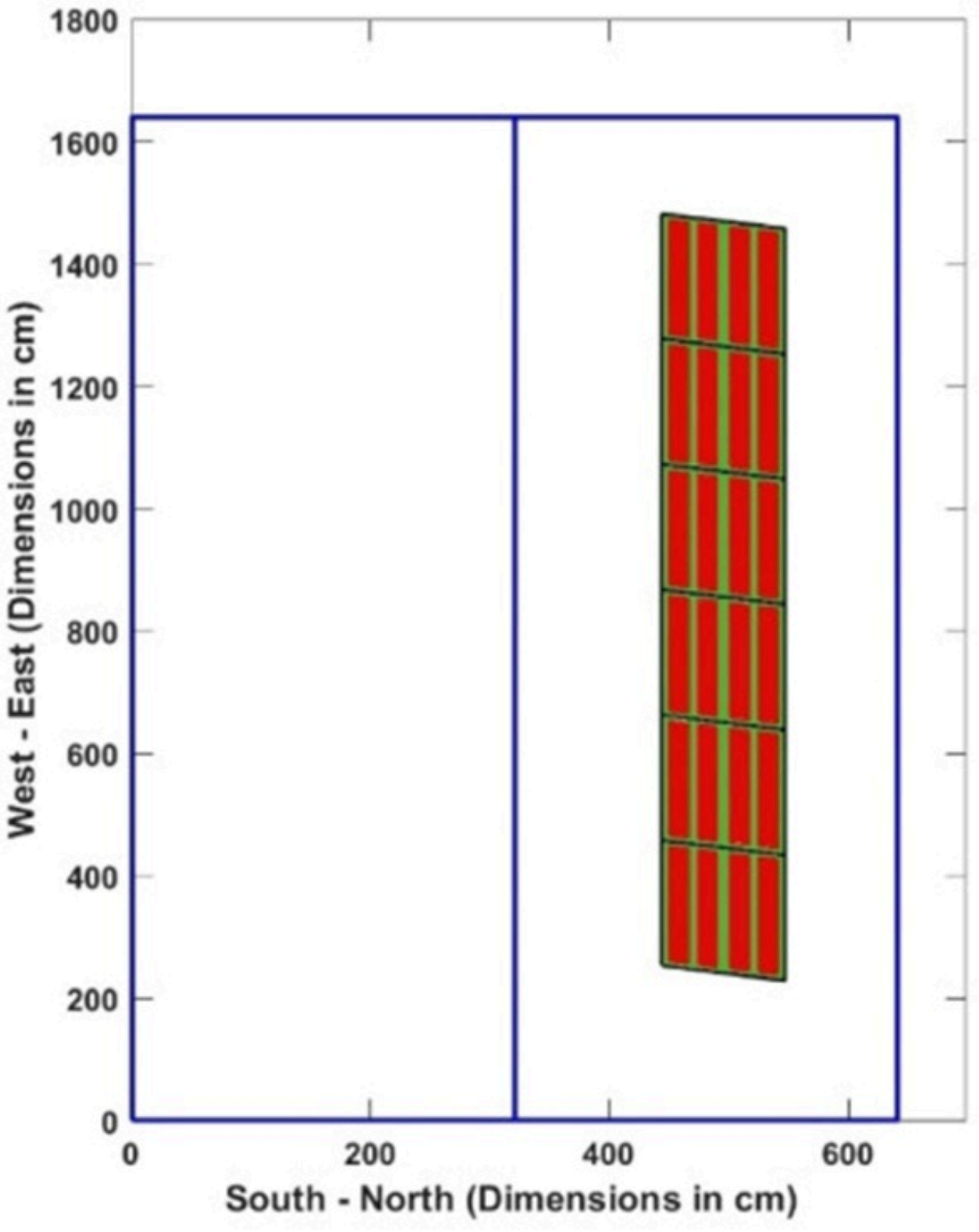

Figure 4. Shadow formed by the PV modules of the northern construction unit: (a) the red zone corresponds to the shadow cast by the solar cells, (b) the green zone corresponds to the influence of the “transparent” segment of the PVs. White space lies outside the PV influence.

© 2024 The Author(s). | Published by Agro Intelligence Research Press

Across all five datasets, Pearson's r coefficients were computed to assess the relationship between solar radiation measured outside the greenhouse and that recorded by Pyranometer 1 and Pyranometer 2. In parallel, p-values were calculated at the 0.05 significance threshold to determine whether the outcomes were statistically significant. Additionally, matching correlation coefficients were calculated for nine clear-sky days sampled from the equivalent quarter of 2022, back when no photovoltaic modules had yet been installed on the greenhouse structure. This step yields a comparative glimpse into the linkage between outdoor and indoor solar radiation, untouched by photovoltaic effects. The physical placement of both pyranometers remained identical in 2022 and 2024.

With respect to the CV, the discrepancy between outdoor solar radiation and the readings from Pyranometers 1 and 2 was first obtained from the logged records. Then, guided by the algorithm's outputs, the data were split according to the following grouping:

(acv) The pyranometers stood clear of any influence from the full surface of the northern construction unit's photovoltaic modules (4570 observations for Pyranometer 1, 5794 for Pyranometer 2).

(bcv) The pyranometers stood within the influence of the full surface of the northern construction unit's photovoltaic modules (3028 observations for Pyranometer 1, 1804 for Pyranometer 2).

(ccv) The pyranometers stood within the influence of the shadow thrown by the solar cells (1936 observations for Pyranometer 1, 1171 for Pyranometer 2).

(dcv) The pyranometers stood within the influence of the "transparent" segment of the relevant PV modules (1092 observations for Pyranometer 1, 633 for Pyranometer 2).

To compute the CVs and to set the coefficients from case (acv) side by side with those from cases (bcv), (ccv), and (dcv) —and acknowledging that the CV inherently reflects sample size—the observations belonging to case (acv) for Pyranometer 1 were broken into:

• 20 randomly selected smaller subsets destined for comparison with the CV of case (bcv)

• 30 randomly selected smaller subsets destined for comparison with the CV of the case (ccv)

• 50 randomly selected smaller subsets destined for comparison with the CV of the case (dcv)

while for Pyranometer 2, the observations belonging to case (acv) were broken into:

• 40 randomly selected smaller subsets destined for comparison with the CV of case (bcv)

• 50 randomly selected smaller subsets destined for comparison with the CV of the case (ccv)

• 100 randomly selected smaller subsets destined for comparison with the CV of the case (dcv)

The number of smaller subsets was settled by taking the observation count from case (acv), dividing it by the observation count from each of cases (bcv), (ccv), and (dcv) in turn, and multiplying each quotient by 10 to span the widest possible range of combinations.

Results and Discussion

Validation results

© 2024 The Author(s). | Published by Agro Intelligence Research Press

As laid out in Section 2.4, two distinct statistical measures were harnessed to authenticate the algorithm—Pearson's r on one side, and the CV on the other. The authentication exercise entailed studying and executing the algorithm over eight clear-sky days, of which three belonged to April (April 20, 2024, April 28, 2024, April 29, 2024), four to May (May 06, 2024, May 22, 2024, May 28, 2024), and three to June (June 01, 2024, June 21, 2024, June 22, 2024).

Figures 5a, 5c, and 5e show representative data collected on April 29, 2024, May 28, 2024, and June 22, 2024, via Pyranometer 1, respectively, whereas **Figure 5b, 5d, and 5g** show the corresponding records from Pyranometer 2. The charts included here plot external radiation, internal radiation measured by the pyranometers, and the algorithm's predictions. Regions colored in red signal the time windows where, according to the algorithm, the pyranometer finds itself beneath the shadow produced by the solar cells, while regions colored in green signal the windows where the pyranometer comes solely under the influence of the "transparent" portion of the photovoltaic surface.

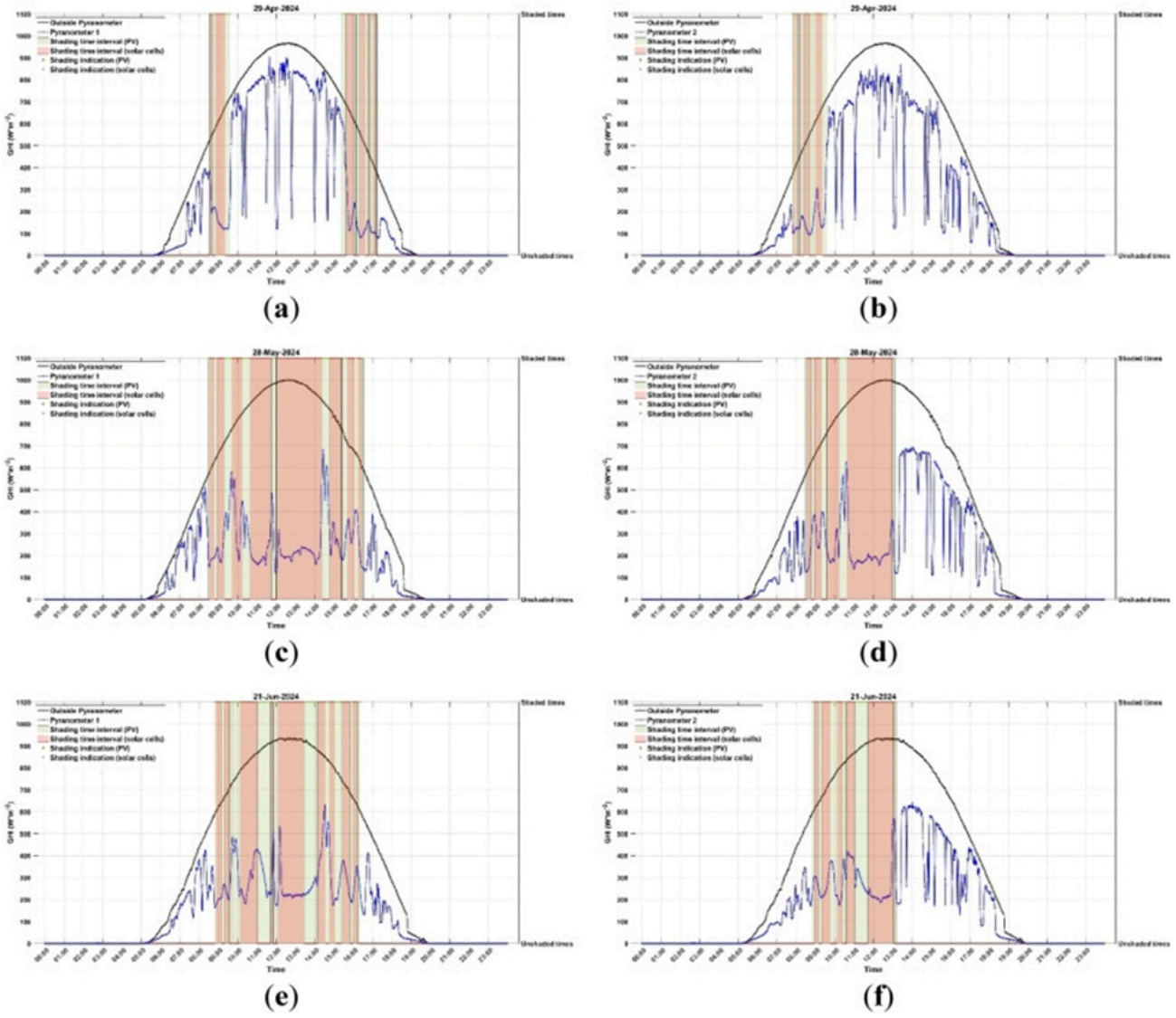

Figure 5. External GHI, internal GHI, and algorithm predictions for April 29, 2024, May 28, 2024, and June 21, 2024, as measured by (a), (c), (e) Pyranometer 1, (b), (d), (f) Pyranometer 2. (Red regions: time windows during which the pyranometer sits beneath the shadow produced by the solar cells. Green regions: time windows during which the pyranometer comes solely under the influence of the "transparent" portion of the photovoltaics.

© 2024 The Author(s). | Published by Agro Intelligence Research Press

Table 2 compiles the correlation coefficient values obtained for the instances when the pyranometers experience or escape the influence of the full PV module surface (cases a1 and a2), when they experience or escape the influence of the shadow originating from the solar cells of those PV modules (cases b1 and b2), and when they come under the influence of the "transparent" segment of the photovoltaics (case c). Every accompanying p-value at the 0.05 significance threshold equals 0, lending statistical significance to the findings.

Table 2. Correlation coefficients across the various shaded and unshaded scenarios for pyranometers 1 and 2.

Case	Pearson's r value
Pyranometer 1	
a1	0.2602
a2	0.9188
b1	0.2550
b2	0.8179
C	0.3408
Pyranometer 2	
a1	0.3261
a2	0.8751
b1	0.2932
b2	0.8296
C	0.4663

Beyond calculating correlation coefficients for 2024, as already mentioned in Section 2.4, coefficients were also derived for nine clear-sky days in 2022, a period before any photovoltaic modules had been installed in the greenhouse. The exact dates did not align perfectly owing to expected differences in weather patterns, which delivered different clear-sky days. Nonetheless, all nine days fell within the April–May–June window, with numerical matching, and pre-sunrise and post-sunset readings were stripped out. The coefficients were 0.9376 for Pyranometer 1 and 0.9256 for Pyranometer 2, with p-values of 0, indicating statistical significance.

Placing the 2022 coefficients alongside those from case a2 for both pyranometers reveals a strong resemblance, reinforcing the idea that no external factor was distorting the radiation within the greenhouse. It also deserves mention that, aside from the addition of photovoltaics to the greenhouse roof, nothing else was changed—neither the cladding nor the structural frame.

Looking next at the contrast between cases a1 and a2, which register values of 0.2602 and 0.9188 for Pyranometer 1 and 0.3261 and 0.8751 for Pyranometer 2, a sizeable gap emerges, confirming the role of an external agent (the PV modules) in substantially reshaping the radiation entering the greenhouse. This large gap also arises because the algorithm tracks only the direct radiation component, which on clear-sky days dominates the diffuse component by a wide margin [24, 25] due to the lack of prominent atmospheric scatterers, such as clouds. The difference grows starker still when contrasting cases a2 and b1, where the radiation correlation is evaluated while, per the algorithm's instructions, the pyranometers are located in a region shadowed by the solar cells rather than entirely beyond the PV modules' reach. The correlation coefficients for case b1 across both pyranometers dip below 0.3, indicating shading and, consequently, the algorithm's correct performance. The coefficients display an upward swing for case c, wherein the pyranometers collect a greater

© 2024 The Author(s). | Published by Agro Intelligence Research Press

fraction of direct radiation permitted through the “transparent” portion of the PV surface. Cases b2 exhibit a sensible decline in correlation coefficients, since the radiation signal blends periods when the pyranometers lie wholly free of any PV shadow together with periods when radiation traverses the “transparent” segment of the PV surface.

Accordingly, aside from demonstrating the algorithm’s accurate outputs, the foregoing discussion also highlights its elevated precision, as evidenced by the coefficient separation between cases b1 and c.

To supplement the use of correlation coefficients for validating the algorithm’s outputs, the CV was also used. This approach was adopted for validating the original algorithm, as discussed in Section 2.4. The CV was not derived straight from the solar radiation values captured by the indoor and outdoor pyranometers; rather, it was anchored in the difference between outdoor and indoor solar radiation. The reasoning behind this choice stems from the seemingly steady figures this quantity shows when the pyranometers are within the photovoltaics’ influence sphere.

The CV figures for cases bcv, ccv, and dcv for Pyranometer 1 were 31.68%, 29.12%, and 34.44%, respectively, while for Pyranometer 2, the corresponding figures were 32.66%, 31.00%, and 33.29%. **Figures 6 and 7** illustrate how cases bcv **(Figures 5a and 6a)**, ccv **(Figures 6b and 6b)**, and dcv **(Figures 6c and 7c)** stack up against case acv, for Pyranometer 1 and Pyranometer 2 alike. Although the magnitudes associated with cases bcv, ccv, and dcv are fixed, the plots depict them fluctuating because each comparison pits the Shaded Set (under photovoltaic influence) against a Random Set drawn from observations in which the pyranometers remain unshaded.

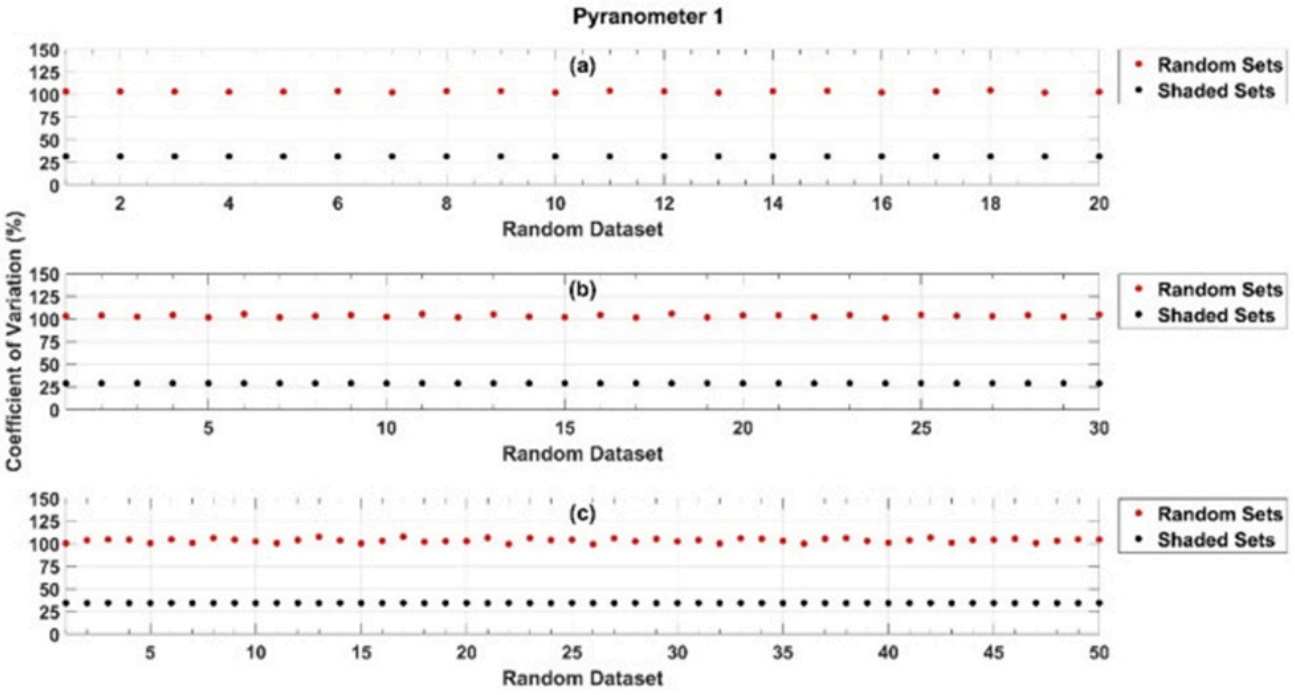

Figure 6. Coefficients of Variation for irradiance-difference datasets comparing (a) case bcv versus acv, (b) case ccv versus acv, and (c) case dcv versus acv for Pyranometer 1.

© 2024 The Author(s). | Published by Agro Intelligence Research Press

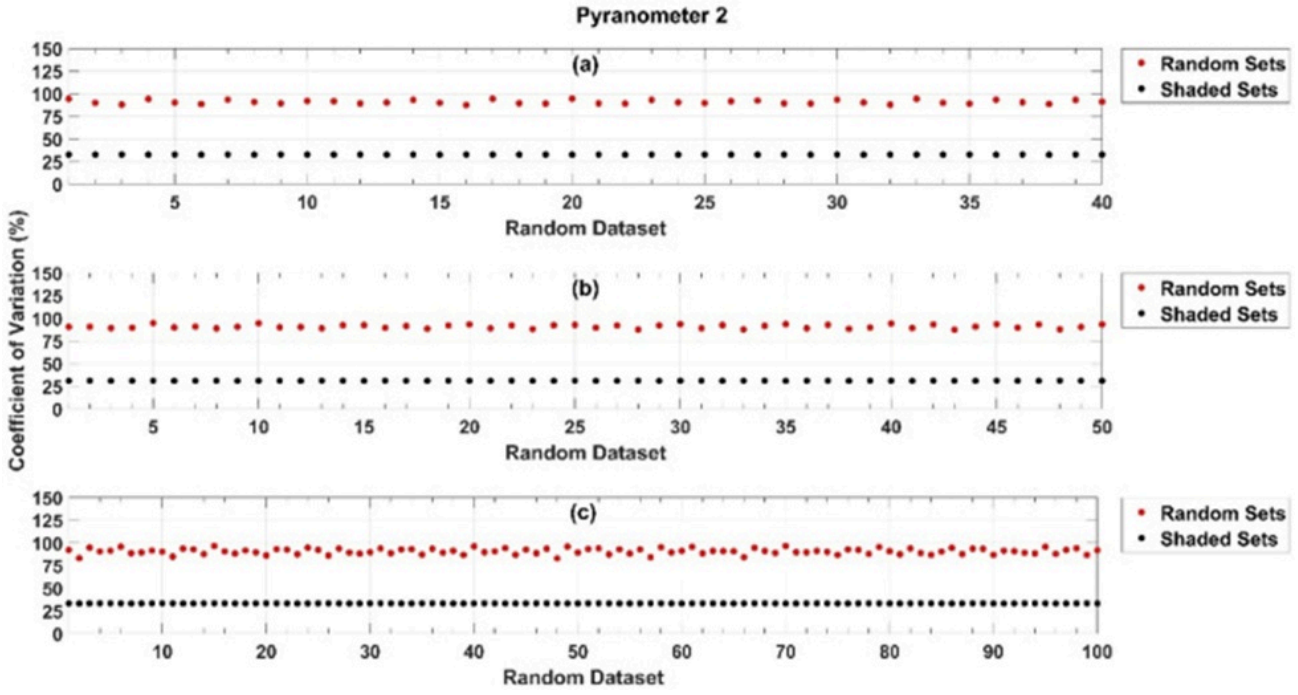

Figure 7. Coefficients of Variation for irradiance-difference datasets comparing (a) case bcv versus acv, (b) case ccv versus acv, and (c) case dcv versus acv for Pyranometer 2.

What the charts in **Figures 6 and 7** reveal for both Pyranometer 1 and Pyranometer 2 is that the CVs tied to case acv remain systematically higher than those tied to cases bcv, ccv, and dcv. In more exact terms, the average CVs recorded when comparing cases bcv, ccv, and dcv are 103.40%, 103.48%, and 103.36% for Pyranometer 1, and 90.82%, 90.72%, and 90.62% for Pyranometer 2, respectively. Such an outcome suggests that the gap between outdoor and indoor radiation exhibits less pronounced fluctuations when the photovoltaic modules are in operation, thereby substantiating the algorithm's sound identification of the shaded footprint. Beyond this, lining up the CVs for cases bcv, ccv, and dcv against one another reveals that the dense shadow thrown by the solar cells clamps the radiation difference at comparatively steady readings—steadier, indeed, than when the pyranometers merely fall under the sway of the "transparent" part of the photovoltaics.

Comparisons for GHI and PAR

Building on the algorithm's output, this study assessed shifts in both GHI and PAR. This evaluation drew upon the logged measurements and the algorithm outputs for the very same days cited in Section 3.1. Once more, the selection favored clear-sky conditions, as these ensure the high direct radiation levels that underpin the algorithm's calculations.

Because of how the sun moves and the geometry of the greenhouse–PV system throughout the day, there are moments when only the instruments placed at position 1 (pyranometer and PAR sensor) experience shading. The corresponding instruments at position 2, in the meantime, remain entirely free of photovoltaic interference, even though the radiation incident on the PV units is identical at both locations.

By way of illustration, **Figures 8a and 8b** show the indoor readings from Pyranometers 1 and 2, respectively, on June 22, 2024, plotted alongside the algorithm's indications of whether photovoltaic module effects are present. **Figures 9a and 9b** provide analogous depictions of PAR within the greenhouse. On the date in question, Pyranometer 1 stays under PV influence for a longer stretch than Pyranometer 2, with the former finally leaving the shaded zone at 16:21. At the same time, the latter clears the shadow roughly three hours earlier, at 13:11. The matching exit times for the PAR sensors are

© 2024 The Author(s). | Published by Agro Intelligence Research Press

16:21 and 13:13, a slight offset rooted in the differing positions of the pyranometers and the PAR sensors. The same procedure was followed for every other day in the dataset.

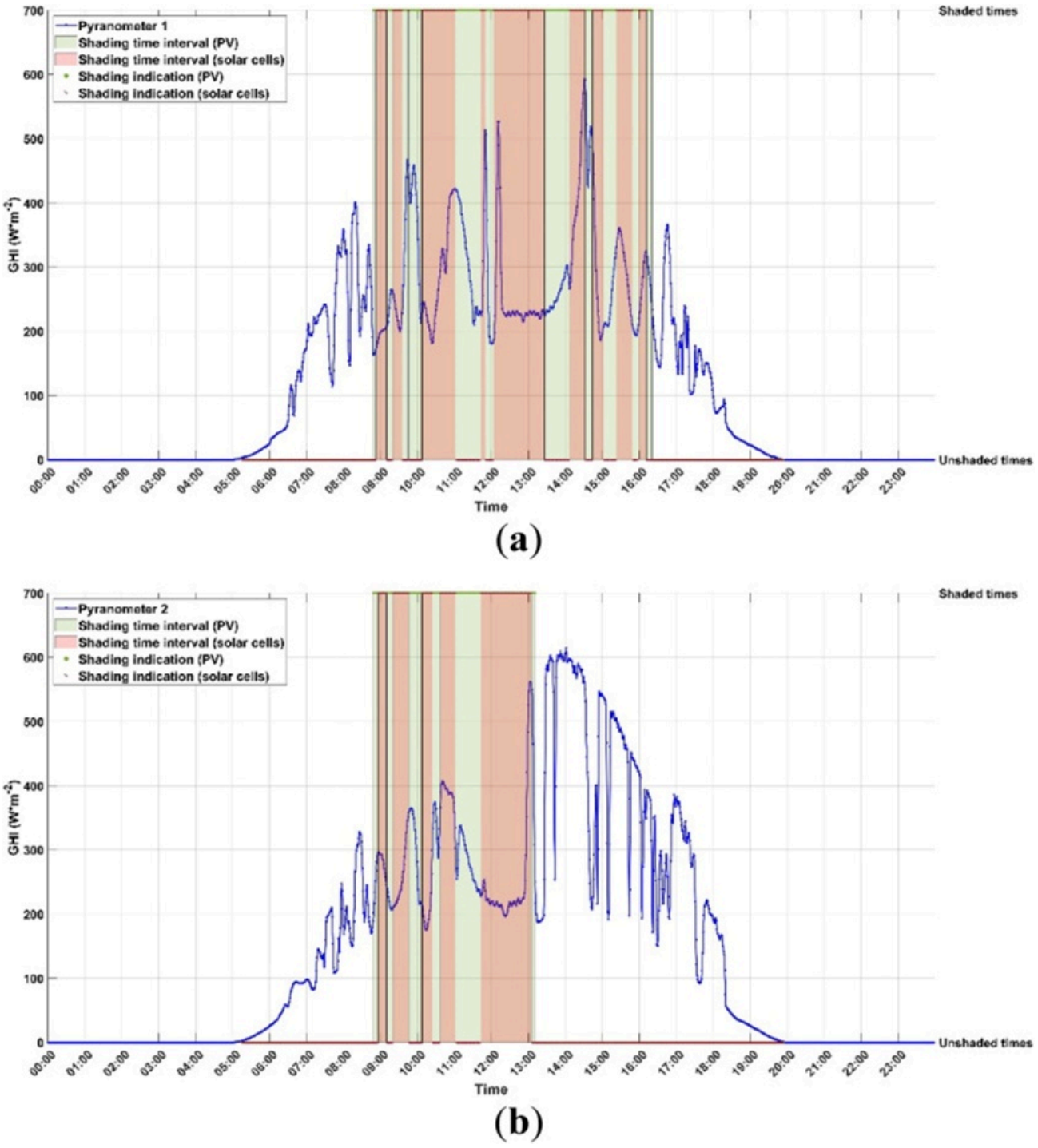

Figure 8. Global Horizontal Irradiance together with shading flag on June 22, 2024, for (a) Pyranometer 1 and (b) Pyranometer 2.

© 2024 The Author(s). | Published by Agro Intelligence Research Press

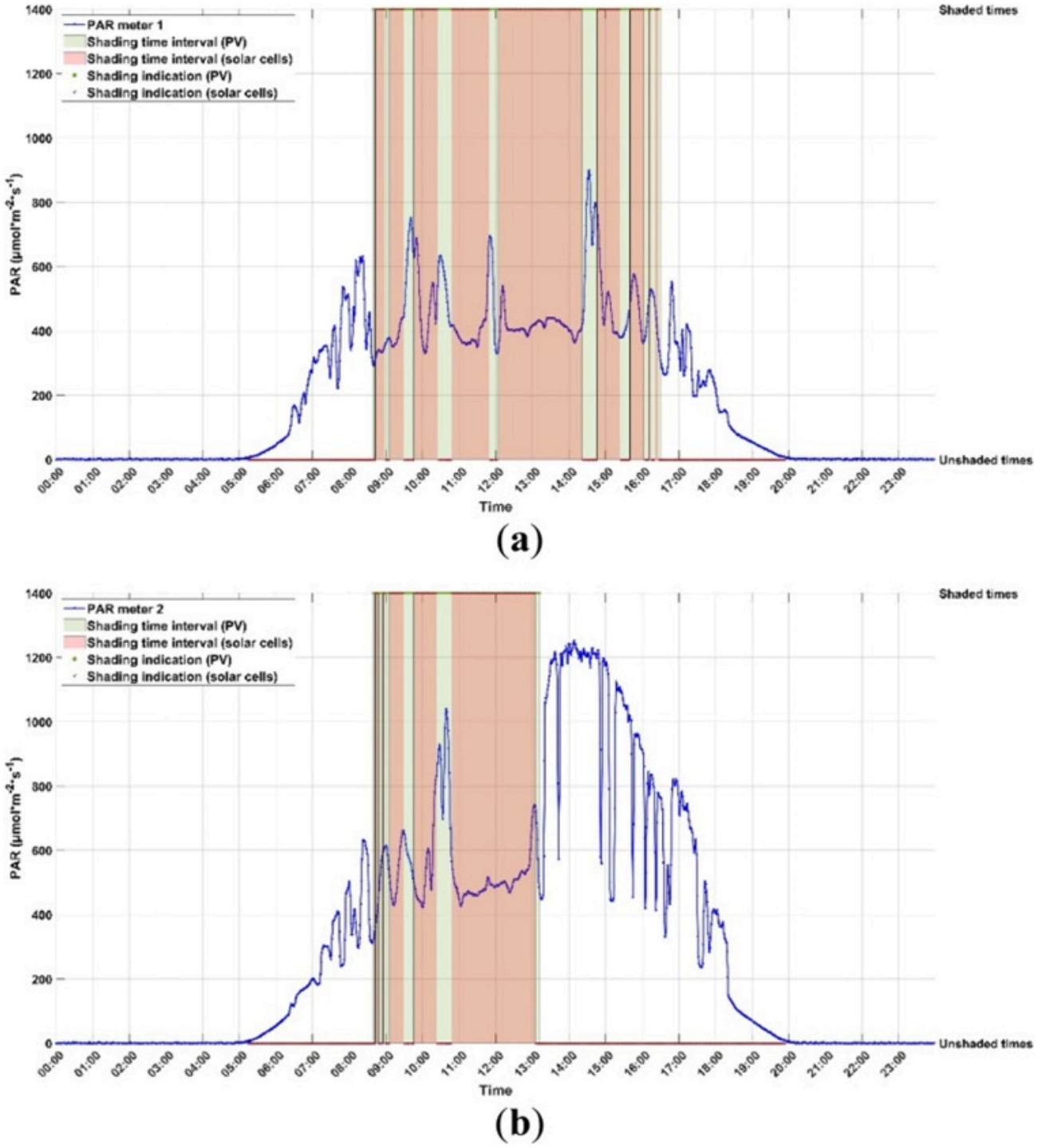

Figure 9. Photosynthetically Active Radiation together with shading flag on June 22, 2024, for (a) Pyranometer 1 and (b) Pyranometer 2.

Radiation comparisons were drawn for three separate scenarios. The algorithm enables isolating the moments when radiation is modified by the solar cells and the “transparent” portion of the photovoltaics. At the same time, it is equally important to quantify the entire photovoltaic surface’s performance. The three scenarios under comparison are therefore:

1. The impact of the solar cells.

© 2024 The Author(s). | Published by Agro Intelligence Research Press

2. The impact of the “transparent” region of the photovoltaics.

3. The impact of the whole photovoltaic surface.

The metrics examined are the mean absolute discrepancy (Mean Absolute Difference – W·m⁻²) between the readings from the two sensors, together with the mean percentage discrepancy (Mean Relative Difference – %). Specifically, **Eq. 13** was employed to determine the mean absolute discrepancy for each scenario, while **Eq. 14** supplied the mean percentage discrepancy.

$$\text{Mean Absolute Difference} = \frac{1}{n}\sum_{i=1}^{n}\left(P_{1,i} - P_{2,i}\right) \quad (13)$$

$$\text{Mean Relative Difference} = \frac{1}{n}\sum_{i=1}^{n}\left(\frac{P_{1,i}-P_{2,i}}{P_{2,i}} \times 100\%\right) \quad (14)$$

Where P1,i and P2,i represent the minute-by-minute GHI or PAR readings gathered by Sensor 1 and Sensor 2, respectively, and n stands for the tally of values falling under each scenario. While deriving the above metrics, any intervals during which skeletal greenhouse components cast shadows on the sensors were excluded.

Table 3 lays out the comparison outcomes for both GHI and PAR.

Table 3. Absolute and relative differences for GHI and PAR.

Metric	Entire surface effect	Transparent section effect	Solar cells effect
GHI–Absolute difference (W·m⁻²)	−269.24	−253.16	−280.68
GHI–Relative difference (%)	−52.51	−51.02	−53.57
PAR–Absolute difference (μmol·m⁻²·s⁻¹)	−628.48	−551.69	−665.06
PAR–Relative difference (%)	−60.26	−53.79	−63.34

The figures in **Table 3** reveal a pronounced dip in radiation, affecting both GHI and PAR. Regarding GHI, the gap between the two pyranometers during stretches when Pyranometer 1 lay shaded by the solar cells, whereas Pyranometer 2 did not reach 280.68 W·m⁻², equivalent to 53.57%; the solar cells blocked roughly 281 W·m⁻² of direct solar radiation. The influence attributable to the “transparent” section of the photovoltaics is less marked by a margin of 27.52 W·m⁻², or 2.73%. The modest scale of this margin suggests there may be scope to integrate additional solar cells across the photovoltaic surface, boosting the active area and, by extension, the energy output.

Although the photovoltaic module layout—specifically the zones devoid of solar cells—permits sunlight scattering that yields better uniformity inside the greenhouse, one must bear in mind that the algorithm computes the shaded footprint resulting from the blockage of sun rays that land squarely on the solar cell surfaces (umbra), without accounting for the partial shadow (penumbra) that forms around the deep shadow of the cells. Taken together with the narrow cell-to-cell spacing and the comparatively large distance from the panels to the pyranometers, the shadowing from the solar cells appears to govern the whole surface that the photovoltaic module would shade if it were opaque. This tallies with the

© 2024 The Author(s). | Published by Agro Intelligence Research Press

mean radiation drop stemming from the full photovoltaic surface, which stands at 269.24 $W \cdot m^{-2}$, or 52.51%—a value that, moreover, diverges only slightly from the numbers recorded for the two earlier scenarios.

Shifting to PAR, a substantial radiation drop is likewise evident, exceeding 50% across all three scenarios. To be precise, the reduction brought on by the solar cells amounts to 665.06 $\mu mol \cdot m^{-2} \cdot s^{-1}$, or 63.34%. By comparison, under the scenario involving the “transparent” region of the photovoltaic, that reduction equals 551.59 $\mu mol \cdot m^{-2} \cdot s^{-1}$, or 53.79%. This gap is wider than observed for total radiation, highlighting the different ways the panels respond to radiation across different wavelength intervals. Here, too, the behavior of the algorithm highlighted in the preceding scenario should be kept in view. The meaningful role of partial shading also emerges in the PAR data; the drop in PAR attributable to the entire photovoltaic surface reaches 628.48 $\mu mol \cdot m^{-2} \cdot s^{-1}$, or 60.26%, a figure that sits very close to the drop tied solely to solar cell shading.

Concerning what these radiation levels mean for potential crops grown under cover, as mentioned by Zhong *et al.* [26], the PAR range considered optimal for strawberry cultivation—a crop commonly produced in greenhouses—lies between 339.6 and 452.8 $\mu mol \cdot m^{-2} \cdot s^{-1}$. The average PAR figures, computed from shading cast by the full photovoltaic panel surface, were roughly 431 $\mu mol \cdot m^{-2} \cdot s^{-1}$ for PAR sensor 1 and roughly 1060 $\mu mol \cdot m^{-2} \cdot s^{-1}$ for PAR sensor 2. Bearing these numbers in mind, one notices that although the PAR reduction caused by the photovoltaic panels is considerable, the lowest recorded value still falls within the optimal window for strawberry growth, suggesting that incorporating photovoltaics into greenhouses could be beneficial for certain crops, such as strawberries. By contrast, as reported by Angmo *et al.* [27], after comparing tomato plants grown in an open field (mean PAR ≈ 1457.4 $\mu mol \cdot m^{-2} \cdot s^{-1}$), inside a standard greenhouse (mean PAR ≈ 836.5 $\mu mol \cdot m^{-2} \cdot s^{-1}$), and inside a shaded greenhouse (mean PAR ≈ 247.9 $\mu mol \cdot m^{-2} \cdot s^{-1}$), it was noted that shading led to a 48% yield reduction. At the same time, fruit quality was higher in the open field. That said, factors beyond radiation—temperature and relative humidity among them—carry considerable weight, suggesting further study is needed to examine how photovoltaics affect those variables.

Challenges in greenhouse shading calculations

As highlighted earlier, the algorithm takes in a broad spectrum of input information, covering the exact moment for which shading is to be computed (year, month, day, hour, minutes, seconds, time zone), the geographic coordinates (latitude and longitude of the greenhouse site), the greenhouse traits (orientation, number of construction units widthwise and lengthwise, width and length of those units, gutter height, and ridge height), the traits of the photovoltaic modules and solar cells (length and width of the module and the cells), the placement of the modules on the roof, and finally, the height at which the shadow is to be sought.

Among these inputs, the model results are shaped by a range of systematic errors, mainly traceable to the greenhouse and photovoltaic module characteristics. It stands to reason that accurately gauging the dimensions of a large greenhouse is far from straightforward. In the present study, all dimensional measurements were taken by conventional means, namely with a measuring tape. Such a method may not be particularly precise, eroding the output precision. This source of error can, however, be reduced or even eliminated by turning to advanced measuring devices—such as laser rangefinders—which provide highly accurate readings even over considerable distances.

Additional errors may creep in during computations of the sun’s position relative to the study site. It warrants emphasis that the most commonly adopted methods for determining the sun’s location require a minimum time step of 1 hour. For a temporal resolution as fine as the one employed here for shading determination (1 min), the calculations require carrying numerous decimal digits. This detail was taken into account when implementing the algorithm.

Finally, a factor that challenges the accuracy of the outputs, particularly when examining solar radiation, is the greenhouse–PV system’s design. Installing photovoltaic modules on the greenhouse roof moves them farther from the surface where the shadow is chiefly evaluated. As noted before, the secondary shadow, coupled with scattered radiation,

© 2024 The Author(s). | Published by Agro Intelligence Research Press

impinges upon result fidelity. This effect shrinks as the gap between the photovoltaic modules and the surface where the shadow forms narrows.

Conclusion

This paper describes refinements and modifications to an algorithm originally developed to identify shading generated by photovoltaic units installed in greenhouses. The initial version was geared toward finding the shadow cast by modules treated as opaque, and its validation was performed under those matching assumptions. After refinement and modification, the algorithm acquired the capability to locate shading from semi-transparent PV units, including the ability to determine whether a given point is shaded solely by solar cells. With this finer-grained shadow representation, it becomes possible to study how the photovoltaic installation affects the direct solar radiation incident on any chosen point within the PV unit.

The algorithm's design is rooted in an actual greenhouse equipped with semi-transparent photovoltaic glass and radiation sensors. The improvements were therefore shaped by the requirements of this experimental setup, while ensuring the tool remains usable in any greenhouse. Among the particularly useful additions are the capacity to resolve shading at various heights within the greenhouse and to operate at tighter time steps, down to one minute. Determining shading during such brief windows may not be essential for cropping, but it is especially valuable for interpreting radiation measurements taken inside the greenhouse. Within a structure containing multiple skeletal components of different cross-sections, the individual shadows become numerous, making a short analysis time step a powerful tool. Finally, the algorithmic changes made it more efficient than its original form; it can now be applied to large-scale greenhouses with only modest computational power.

The updated algorithm version was validated using two metrics: Pearson's r and the CV. With respect to Pearson's r, the validation findings indicated that the correlation between indoor and outdoor GHI is especially low when the algorithm reports interference from the solar cells. In contrast, when radiation passed through only the greenhouse glass cover, the correlation between the various GHI measurements was considerably higher, with values at the same time approaching those computed for intervals when no photovoltaics were on the roof. As for the CV, the figures for the gap between outdoor and indoor GHI were lower when the GHI was under photovoltaic influence than when it was not. This outcome aligns with the findings obtained for the original, already-validated algorithm.

Afterward, with the algorithm's help, time windows were identified during which shading from the photovoltaics affected only one pyranometer (and one PAR sensor) due to shadowing. Taking advantage of this situation, the effects of photovoltaics on GHI and PAR were examined. The findings showed that shading from the solar cells reduced GHI by roughly 53% and PAR by about 63%. Yet the influence of the "transparent" portion of the photovoltaics was also significant, resulting in reductions of 51% in GHI and 54% in PAR.

That being said, within a photovoltaic greenhouse and at the operational–commercial scale for greenhouse crops, the scenario values to be considered are those reflecting the radiation impact of the entire photovoltaic surface (a reduction of 52.51% for GHI and 60.26% for PAR). These numbers may turn out to be either beneficial or detrimental, depending on the requirements of each case—such as the crop type and the amount of sunlight it needs, or the necessity to cool the greenhouse, most critically during the summer months.

In closing, thanks to the algorithm, it is now possible to study the radiation conditions inside the greenhouse beneath panels of different kinds—panels that differ either in the arrangement of solar cells across their surface or in the construction material that chiefly determines the radiation passing through the "transparent" region of the photovoltaic unit. At the same time, by deploying the algorithm and detecting shading patterns, one can now investigate other microclimatic parameters, such as the temperature distribution across different zones within a greenhouse. Finally, given the algorithm's structure (functions and separate code fragments) and the modifications and additions presented above,

© 2024 The Author(s). | Published by Agro Intelligence Research Press

applying it at a larger scale is now feasible, and extending it to open-field crops is also possible, broadening its utility within the Agrivoltaics arena.

Acknowledgements

The present work was financially supported by the «Andreas Mentzelopoulos Foundation».

Conflict of interest

None

Financial support

This paper was funded in the framework of “Pilot application of greenhouse simulation of indigenous climatic conditions for the cultivation of Aloe (*Aloe Vera*) for optimal production of Acemannan polysaccharide”. M16SYN2-00282. Sub-measure 16.1–16.2 “Establishment and operation of Operational Groups of the European Innovation Partnership for agricultural productivity and sustainability”, Action 2, of the Rural Development Programme 2014-2020 (RDP 407 2014-2020), Region of Western Greece, December 2022 – 2024.

Ethics statement

None

Received: 06 Jan 2023 Revised: 13 Mar 2023 Accepted: 29 Mar 2023
Published online: 25 May 2024

Rights and permissions

Open Access The author(s) retain copyright. This article is licensed under the Creative Commons Attribution-NonCommercial-ShareAlike 4.0 International License. It may be shared and adapted for non-commercial purposes with appropriate attribution, an indication of changes, and distribution of adaptations under the same license. Third-party material may be subject to separate terms identified in its credit line. View the license at https://creativecommons.org/licenses/by-nc-sa/4.0/.

References

1. Petrakis T, Thomopoulos V, Kavga A, Argiriou A. An algorithm for calculating the shade created by greenhouse integrated photovoltaics. Energy Ecol Environ. 2023. https://doi.org/10.1007/s40974-023-00306-4.

2. Widmer J, Christ B, Grenz J, Norgrove L. Agrivoltaics, a promising new tool for electricity and food production: A systematic review. Renew Sustain Energy Rev. 2024;192:114277. https://doi.org/10.1016/j.rser.2023.114277.

3. Chatzipanagi A, Taylor N, Jaeger-Waldau A. Overview of the potential and challenges for agri-photovoltaics in the European Union. Sci Anal Rev. 2023. Policy Assessment KJ-NA-31-482-EN-N. Luxembourg (Luxembourg). https://doi.org/10.2760/208702.

4. Abdel-Ghany A, Al-Helal I, Alkoaik F, Alsadon A, Shady M, Ibrahim A. Predicting the cooling potential of different shading methods for greenhouses in arid regions. Energies (Basel). 2019;12. https://doi.org/10.3390/en12244716.

5. Caruso G, Formisano L, Cozzolino E, Pannico A, El-Nakhel C, Rouphael Y, et al. Shading affects yield, elemental composition and antioxidants of perennial wall rocket crops grown from spring to summer in southern Italy. Plants. 2020;9. https://doi.org/10.3390/plants9080933.

6. Yang M, Liu M, Lu J, Yang H. Effects of shading on the growth and leaf photosynthetic characteristics of three forages in an apple orchard on the Loess Plateau of eastern Gansu, China. PeerJ. 2019;7:e7594. https://doi.org/10.7717/peerj.7594.

7. Li H, Jiang D, Wollenweber B, Dai T, Cao W. Effects of shading on morphology, physiology and grain yield of winter wheat. Eur J Agron. 2010;33:267-75. https://doi.org/10.1016/j.eja.2010.07.002.

8. Petrakis T, Ioannou P, Kitsiou F, Kavga A, Grammatikopoulos G, Karamanos N. Growth and physiological characteristics of strawberry plants cultivated under greenhouse-integrated semi-transparent photovoltaics. Plants. 2024;13. https://doi.org/10.3390/plants13060768.

9. McCree KJ. The action spectrum, absorptance and quantum yield of photosynthesis in crop plants. Agric Meteorol. 1971;9:191-216. https://doi.org/10.1016/0002-1571(71)90022-7.

10. Hosseini A, Zare Mehrjerdi M, Aliniaeifard S, Seif M. Photosynthetic and growth responses of green and purple basil plants under different spectral compositions. Physiol Mol Biol Plants. 2019;25:741-52.

11. Pennisi G, Orsini F, Blasioli S, Cellini A, Crepaldi A, Braschi I, et al. Resource use efficiency of indoor lettuce (Lactuca sativa L.) cultivation as affected by red:blue ratio provided by LED lighting. Sci Rep. 2019;9:14127. https://doi.org/10.1038/s41598-019-50783-z.

12. Jin D, Su X, Li Y, Shi M, Yang B, Wan W, et al. Effect of red and blue light on cucumber seedlings grown in a plant factory. Horticulturae. 2023;9.

13. López-Díaz G, Carreño-Ortega A, Fatnassi H, Poncet C, Díaz-Pérez M. The effect of different levels of shading in a photovoltaic greenhouse with a North–South orientation. Appl Sci. 2020;10. https://doi.org/10.3390/app10030882.

14. Cossu M, Yano A, Solinas S, Deligios PA, Tiloca MT, Cossu A, et al. Agricultural sustainability estimation of the European photovoltaic greenhouses. Eur J Agron. 2020;118:126074. https://doi.org/10.1016/j.eja.2020.126074.

15. Barbera E, Sforza E, Vecchiato L, Bertucco A. Energy and economic analysis of microalgae cultivation in a photovoltaic-assisted greenhouse: Scenedesmus obliquus as a case study. Energy. 2017;140:116-24.

16. Tang Y, Li M, Ma X. Study on photovoltaic modules on greenhouse roof for energy and strawberry production. E3S Web Conf. 2019;118:03049.

17. Zisis C, Pechlivani E, Tsimikli S, Mekeridis E, Laskarakis A, Logothetidis S. Organic photovoltaics on greenhouse rooftops: Effects on plant growth. Mater Today Proc. 2019;19:65-72. https://doi.org/10.1016/j.matpr.2019.07.658.

© 2024 The Author(s). | Published by Agro Intelligence Research Press

18. Torrente CJ, Reca J, López-Luque R, Martínez J, Casares FJ. Simulation model to analyze the spatial distribution of solar radiation in agrivoltaic Mediterranean greenhouses and its effect on crop water needs. Appl Energy. 2024;353:122050. https://doi.org/10.1016/j.apenergy.2023.122050.

19. Pérez-Alonso J, Pérez-García M, Pasamontes-Romera M, Callejón-Ferre A. Performance analysis and neural modelling of a greenhouse integrated photovoltaic system. Renew Sustain Energy Rev. 2012;16:4675-85. https://doi.org/10.1016/j.rser.2012.04.002.

20. Brite Solar (nd). BSG-250-49 Product Data Sheet. https://www.britesolar.com/uploads/originals/1/bsg-250-49.pdf (Accessed: 13 July 2024). Google Scholar

21. Matkowski H, Daszkowska-Golec A. Update on stomata development and action under abiotic stress. Front Plant Sci. 2023;14. https://doi.org/10.3389/fpls.2023.1270180.

22. Kollist H, Zandalinas SI, Sengupta S, Nuhkat M, Kangasjärvi J, Mittler R. Rapid responses to abiotic stress: Priming the landscape for the signal transduction network. Trends Plant Sci. 2019;24:25-37. https://doi.org/10.1016/j.tplants.2018.10.003.

23. Qu M, Hamdani S, Bunce JA. The physiology and genetics of stomatal adjustment under fluctuating and stressed environments. In: Najafpour MM, editor. Applied Photosynthesis. IntechOpen; 2016. Chapter 4. https://doi.org/10.5772/62223.

24. Rachid A, Goren A, Becerra V, Radulovic J, Khanna S. Fundamentals of solar energy. In: Solar Energy Engineering and Applications. Cham: Springer International Publishing; 2023. p. 1-15.

25. Agbo EP, Ettah EB, Edet CO, Ndoma EG. Characteristics of various radiative fluxes: Global, tilted, direct, and diffused radiation—A case study of Nigeria. Meteorol Atmos Phys. 2023;135:14. https://doi.org/10.1007/s00703-023-00951-8.

26. Zhong P, Yang S, Qiao R, Wang T. Effect of light intensity on main quality of strawberry. Southwest China J Agric Sci. 2011;24(3):1219-21.

27. Angmo P, Phuntsog N, Namgail D, Chaurasia OP, Stobdan T. Effect of shading and high temperature amplitude in greenhouse on growth, photosynthesis, yield and phenolic contents of tomato (Lycopersicum esculentum Mill.). Physiol Mol Biol Plants. 2021;27(7):1539-46. https://doi.org/10.1007/s12298-021-01032-z.

© 2024 The Author(s). | Published by Agro Intelligence Research Press